Breakdown of Classical Kinematic Continuity Conditions at Cracked Cross-Sections of Nanobeams

Akbar Hassanpour, Hossein Darban[1]

Institute of Fundamental Technological Research, Polish Academy of Sciences, Pawińskiego 5B, 02-106 Warsaw, Poland

Abstract

In the existing literature, the effect of a crack in a nanobeam is commonly modeled by introducing a discontinuity in the slope at the cracked cross-sections, with the magnitude proportional to the bending moment transmitted through the section. The proportionality factor (i.e., the crack compliance) is typically derived from closed-form solutions based on classical linear elastic fracture mechanics, whose validity at micro- and nanoscale dimensions is not well established. At such small scales, atomic interactions across crack surfaces become significant and can strongly influence the kinematic fields at the cracked cross-section. Consequently, the accuracy of the majority of existing models for the mechanical behavior of cracked micro- and nanobeams remains unclear. This study examines size effects on the crack compliance of silicon nanobeams by integrating molecular dynamics simulations with beam formulations derived from a nonlocal theory. Size-dependent bending and free-vibration responses of intact nanobeams are first obtained through molecular dynamics simulations, and these results are used to calibrate the nonlocal parameters of the continuum models. The calibrated models are then employed to study cracked nanobeams. Comparisons between molecular dynamics predictions and theoretical results reveal pronounced size effects: classical formulas substantially underestimate crack-induced flexibility in nanobeams, while the discrepancy decreases with increasing beam length. For sufficiently long nanobeams, crack compliance converges toward classical predictions. These results provide direct atomistic evidence that classical kinematic continuity conditions at cracked cross sections are not generally valid at small scales and must be reformulated to accurately capture the mechanical behavior of nanobeams.

[1]- ***Corresponding author:*** *Hossein Darban*; ***E-mail addresses:*** *hdarban@ippt.pan.pl*; ***Tel.:*** *(+48) 22 826 12 81*

Keywords: Crack compliance, Nanobeams, Size effect, Molecular dynamics, Nonlocal elasticity theory.

1. Introduction

The growing field of miniaturization has placed micro- and nanoscale systems and devices at the forefront of innovation. Micro- and nanostructures, such as miniaturized beams, shells, and plates, have attracted significant attention in recent decades due to their critical role in emerging micro- and nanoscale technologies [1,2]. These small-scale structures are increasingly employed in the micro- and nano-electromechanical systems (MEMS and NEMS) for a wide range of applications in aerospace, biomedical, automotive, and civil engineering [3–9]. In MEMS and NEMS, electrical components are integrated with miniaturized mechanical elements to perform critical functions, including chemical sensing [10], micro-electro-mechanical switching [11–14], resonant oscillation and frequency generation [15–18], mass detection [19,20], biosensing [21,22], force measurement [23] and light detection [24,25]. However, small-scale structures are susceptible to defects such as cracks, which can significantly reduce their stiffness and natural frequencies.

Structural health monitoring (SHM) is essential for ensuring the safety, reliability, and serviceability of structural components. A key aspect of SHM is crack detection, as cracks introduce local flexibility, reduce structural stiffness and natural frequencies, and alter both static and dynamic behaviors. Therefore, accurately identifying crack location and depth is crucial for assessing structural integrity and preventing failures. Numerous damage detection techniques have been developed to ensure the safety and integrity of mechanical structures. Among them, vibration-based methods [26,27], wave propagation methods [28,29], and static deflection-based methods [30,31] are commonly used.

In problems involving mechanical elements such as beams, cracks are often modeled as massless elastic springs [32–36]. In this method, the cracked beam is represented as two sub-beams joined at the crack location by rotational and translational springs. The compliances of these elastic springs are then determined using classical fracture mechanics principles, which rely on local elasticity theory. However, these formulas for calculating crack compliances do not account for the size effect. While several pioneering theories based on non-classical continuum mechanics have been developed to address mechanical problems at small scales, e.g., [37–42], size-independent formulas are still frequently used to determine crack compliances of these small-scale

structures, e.g., [43–49]. This discrepancy raises a critical question: how significant is the size effect on crack compliances in nanostructures?

This study aims to address this question by exploring the size effect on crack compliance in small-scale beams under static bending and free transverse vibration. For this purpose, the local/nonlocal stress-driven gradient elasticity (SDGE) model [50] is employed along with molecular dynamics (MD) simulations. The SDGE model is an accurate, well-posed, and computationally efficient approach for addressing size effects in miniaturized structures, providing a robust framework for capturing size-dependent mechanical behavior [51–54]. Nevertheless, any alternative nonlocal beam model may be employed for the purposes of this article, such as those developed in [55–59]. Additionally, MD simulations offer a detailed atomistic perspective on the response of nanostructures. MD has been widely used to investigate a broad range of problems, including the mechanical behavior of nanocrystalline metals, high-entropy alloys and composites [60–65], size-dependent mechanical responses of silicon nanobeams [66], crack growth under cyclic loading [67], and the mechanical properties of carbon nanotubes [68].

The structure of the paper is as follows. Section 2 introduces the problem and outlines the classical evaluation of crack compliance and the SDGE model used to analyze the bending and free transverse vibration of nanobeams. Section 3 describes the MD simulations of intact and cracked silicon nanobeams. Section 4 presents and discusses the results, including calibration SDGE models based on MD data and an investigation of size effects on crack compliance. Section 5 concludes the paper with a summary of the main findings.

2. Problem definition and assumptions

To examine the size effect on crack compliance, an Euler-Bernoulli nanobeam with rectangular cross-section containing one edge crack is considered. A fixed–guided nanobeam for bending and a cantilever nanobeam for free transverse vibration are studied, as illustrated in Fig. 1(a) and Fig. 1(b), respectively. Each beam has an in-plane thickness of H, an out-of-plane width of W, a length of L, and a cross-sectional area of A. A Cartesian coordinate system $x-y$ is established at the mid-thickness of the beam, with the origin at the left end. The crack has a length of a_1 and is located at the position x_1 along the length of the beam. The local bending compliance of the beam

is given by $C = \frac{1}{EI}$, where E is the Young's modulus and I is the second moment of the area, defined as $I = \frac{WH^3}{12}$. The mass per unit length is denoted by I_0, and $I_2 = \frac{I_0 H^2}{12}$.

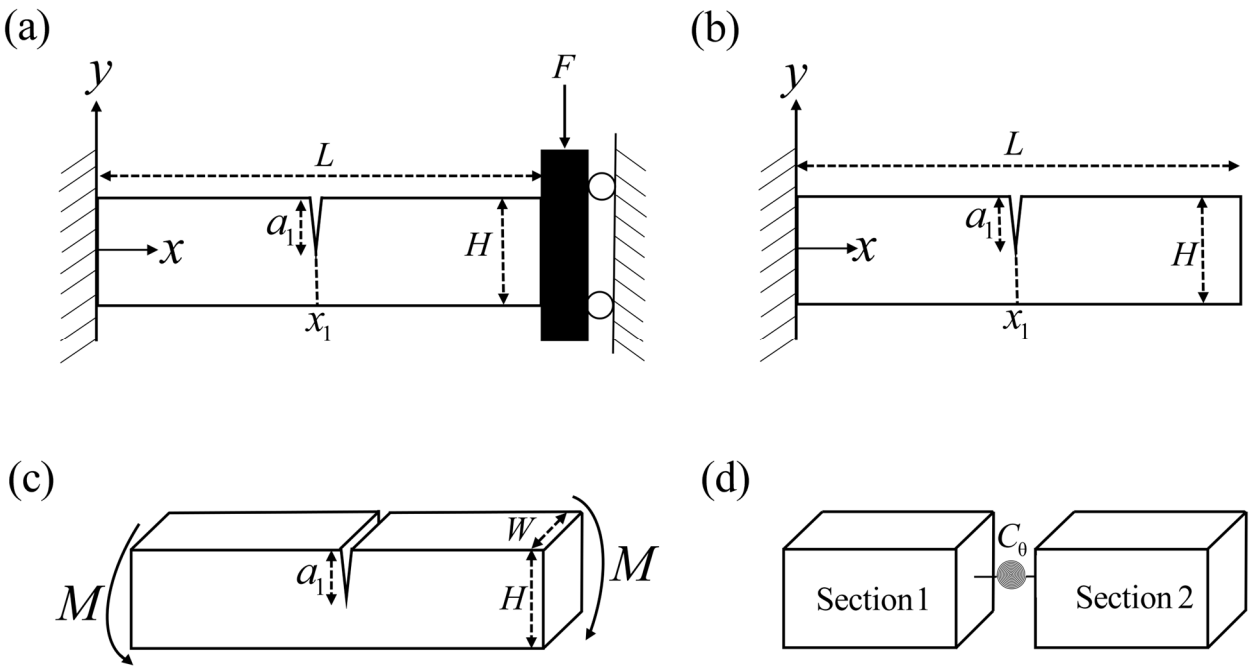

Fig. 1 (a) Fixed–guided cracked nanobeam considered for bending analysis. (b) Cantilever cracked nanobeam considered for free vibration analysis. (c) Mode I deformation induced by bending moment, and (d) modeling a crack by a rotational elastic spring.

2.1. Classical formulation of crack compliance

This section summarizes the classical formulation for the crack compliance developed in [69]. To investigate the mechanics of beams containing edge cracks, the elastic spring model, illustrated in Fig. 1(c) and Fig. 1(d), is commonly employed. In this approach, a cracked slender beam can be modeled by considering two beam segments connected through a massless elastic rotational spring located at the cracked section, with compliance C_θ. The impact of the crack on the static and dynamic behavior of the structure is accounted for by introducing discontinuity in the cross-section rotation $(\theta = \theta_2 - \theta_1)$ at the crack location. This discontinuity is proportional to the bending moment (M) transmitted across the cracked section:

$$\theta = C_\theta M_{crack} \tag{1}$$

The crack compliance is derived by equating the mode I strain energy release rate from fracture mechanics to that associated with the equivalent rotational spring [69]:

$$G = \frac{K_I^2}{E'} = \frac{M^2}{2W}\frac{dC_\theta}{da} \tag{2}$$

Where $E' = E$ for plane stress, and $E' = \frac{E}{1-\nu^2}$ for plane strain.

Using Eq.(2), the rotational compliance C_θ can be written as [69]:

$$C_\theta = \frac{2W}{E'}\int_0^a (\frac{K_I}{M})^2 da \tag{3}$$

The stress intensity factor K_I, which can be found in fracture mechanics handbooks, is given as:

$$\begin{aligned} K_I &= \frac{6M}{WH^2}\sqrt{\pi a}\, F_M(\xi) \qquad \text{for} \quad 0 \le \xi \le 0.6 \\ K_I &= \frac{3.99M}{WH^{3/2}\sqrt{(1-\xi)^3}} \qquad \text{for} \quad 0.6 < \xi < 1 \end{aligned} \tag{4}$$

Here, $\xi = \frac{a}{H}$ is the normalized crack length, and $F_M(\xi)$ is a dimensionless correction function which captures the crack-geometry effects, given by:

$$F_M(\xi)=\sqrt{(\frac{2}{\pi\xi})\tan\frac{\pi\xi}{2}}\left(\frac{0.923+0.199(1-\sin\frac{\pi\xi}{2})^4}{\cos\frac{\pi\xi}{2}}\right) \tag{5}$$

Replacing K_I from Eq.(4) into Eq.(3) results in the following expressions for C_θ:

$$C_\theta=12CH\int_0^\xi R_M^2(\xi)d\xi \qquad \text{for} \quad 0\le\xi\le 0.6$$

$$R_M(\xi)=\sqrt{\tan\frac{\pi\xi}{2}}\left(\frac{0.923+0.199(1-\sin\frac{\pi\xi}{2})^4}{\cos\frac{\pi\xi}{2}}\right) \tag{6}$$

$$C_\theta=2.6535CH\int_0^\xi\frac{1}{(1-\xi)^3}d\xi \qquad \text{for} \quad 0.6<\xi<1$$

The foregoing expression for the crack compliance C_θ depends on the normalized crack length ξ as well as on the material properties and the beam geometry. However, because it contains no intrinsic or small-scale parameters, it is unable to capture size effects and therefore is size-independent.

2.2. The SDGE theory

To address the bending and free transverse vibration problems of nanobeams, the SDGE theory is applied within the framework of Euler-Bernoulli beam theory. The original dynamic integral representation of the SDGE model is given by [50]:

$$\frac{\chi(x,t)}{C}=\alpha M(x,t)+(1-\alpha)\int_0^L \phi_{L_C}(x-\zeta)M(\zeta,t)\,d\zeta - L_l^2\frac{\partial}{\partial x}\int_0^L \phi_{L_C}(x-\zeta)\frac{\partial M(\zeta,t)}{\partial \zeta}d\zeta \tag{7}$$

where χ and M represent the elastic curvature and bending moment, respectively. The constitutive equation formulated by the SDGE theory includes three nonlocal parameters: material length scale parameter (L_C), gradient length scale parameter (L_l), and mixture parameter (α). Additionally, ϕ_{L_C} is a kernel function which depends on the material length scale parameter L_C and defined as:

$$\phi_{L_C}(x)=\frac{1}{2L_C}e^{(-\frac{|x|}{L_C})} \tag{8}$$

The free transverse vibration problem of small-scale beams based on the SDGE theory was previously solved in [70], with relevant details provided in Appendix A. Incorporating the SDGE theory into the Euler–Bernoulli beam framework yields the following governing differential equations for each segment of the nanobeam, including a single edge crack:

$$L_C^2\frac{d^6v_k}{dx^6}-\frac{d^4v_k}{dx^4}+C(\alpha L_C^2+L_l^2)\omega^2\frac{d^4V_k}{dx^4}-(CI_2+CI_0(\alpha L_C^2+L_l^2))\omega^2\frac{d^2V_k}{dx^2}+CI_0\omega^2V_k=0 \tag{9}$$

for k = 1 and 2.

The SDGE model for free transverse vibration of Euler–Bernoulli small-scale beams with a single edge crack yields two governing differential equations of total order 12. Solving this system requires four constitutive conditions (two boundary and two continuity) in addition to eight variationally consistent conditions (four boundary and four continuity). The full set of governing equations, boundary and continuity conditions, and the solution procedures for both static and dynamic analyses are provided in Appendix A.

For the vibration problem of a cracked cantilever nanobeam (see Fig. 1(b)), the system of governing differential equations, together with the required continuity and boundary conditions, results in a homogeneous system of 12 algebraic equations for 12 unknown constants. A non-

trivial solution exists only when the determinant of the coefficient matrix vanishes, yielding the characteristic equation for determining the natural frequencies. The roots of this characteristic equation, i.e., the natural frequencies, are then computed numerically using the bisection method.

For the bending problem of a cracked fixed-guided nanobeam (see Fig. 1(a)), the solution is obtained directly from the dynamic formulation by removing all time-dependent terms. The formulation is presented in Appendix A. For the bending problem of a fixed–guided nanobeam "without" a crack, the governing differential equations, together with the specified boundary and continuity conditions, can be solved to yield the following closed-form solution for the bending stiffness:

$$K_{\mathrm{SDGE}} = \frac{A}{B_1 + B_2 + B_3}$$

where

$$\begin{aligned}
A &= \left(((\alpha-1)L_C + L)e^{\frac{L}{L_C}} - (\alpha-1)L_C \right) H^3 WE \\
B_1 &= \begin{pmatrix} -12(\alpha-1)^2 L_C^4 - 12(\alpha-1)^2 L_C^3 L + (-3(\alpha-1)^2 L^2 + 12L_l^2 - 12\alpha L_l^2)L_C^2 \\ + L_l^2(6-6\alpha)LL_C \end{pmatrix} e^{-\frac{L}{L_C}} \\
B_2 &= \begin{pmatrix} -12(\alpha-1)^2 L_C^4 + (12\alpha-12)LL_C^3 + (3(\alpha-1)^2 L^2 + 12L_l^2 - 12\alpha L_l^2)L_C^2 \\ + ((-4+4\alpha)L^3 + L_l^2(-18+6\alpha)L)L_C + 6L^2 L_l^2 + L^4) \end{pmatrix} e^{\frac{L}{L_C}} \\
B_3 &= \begin{pmatrix} 24(\alpha-1)^2 L_C^4 + (12\alpha^2 - 12\alpha)LL_C^3 + ((12\alpha-12)L^2 + 24\alpha L_l^2 - 24L_l^2)L_C^2 \\ + ((2\alpha-2)L^3 + 12LL_l^2)L_C + 6L^2 L_l^2 \end{pmatrix}
\end{aligned} \tag{10}$$

This equation is a function of the nanobeam dimensions and includes three nonlocal parameters, namely L_C, L_l and α.

3. Molecular dynamics simulations

The MD simulations are performed using the Large Scale Atomic/Molecular Massively Parallel Simulator (LAMMPS) [71] to investigate the mechanical behavior of a series of silicon nanobeams with various lengths while maintaining a constant aspect ratio. All nanobeams have a square cross-section with $W = H = L/12$, where the beam length L ranges from 26.07 nm to 182.48 nm. The nanobeams are constructed from single-crystal silicon with a diamond cubic lattice structure and a lattice constant of 0.5431 nm. The silicon lattice structure is oriented such that the *x*-axis corresponds to the $[1\ 1\ 1]$ crystallographic direction along the beam length, while the *y*-axis and *z*-axis align with the $[\bar{1}\ 2\ \bar{1}]$ and $[\bar{1}\ 0\ 1]$ crystallographic directions, respectively.

In this study, Stillinger-Weber (SW) potential [72] is employed. The SW potential is particularly suitable for covalently bonded materials with diamond cubic structure such as silicon, providing both computational efficiency and accuracy for studying the mechanical behavior of small-scale silicon structures. It incorporates both two-body and three-body interactions, enabling the capture of bond stretching and angular interactions. For silicon, the parameters of the SW potential were originally calibrated to reproduce key thermodynamic, structural, and elastic properties, including the equilibrium behavior at 0 K and the melting temperature. The specific parameter values used in this work are listed in Table 1.

Table 1

Parameter set of the SW potential for silicon, calibrated to reproduce structural and thermodynamic properties [72].

ε (eV)	σ (Å)	a	λ	γ	$\cos\theta_0$	A	B	p	q
2.1683	2.0951	1.80	21.0	1.20	-1/3	7.049556277	0.6022245584	40	0.0

The *A*, *B*, *p*, and *q* parameters are used exclusively in the two-body interaction terms. The λ and $\cos\theta_0$ parameters apply only to the three-body interactions. The *a*, ε and σ parameters are shared by both the two-body and three-body terms. The γ parameter is used only in the three-body interaction but is specified for each interacting pair of atom types. All parameters without explicit physical dimensions are dimensionless.

The MD simulations are conducted in a 3D domain with non-periodic boundary conditions in all directions, and a time step of 1 fs. After the initial atomic configuration of the nanobeam is created, the system energy is minimized using the conjugate gradient algorithm. The nanobeam is then

equilibrated for 100 ps at a temperature of 1 K using the canonical NVT ensemble with a Nose–Hoover thermostat. After equilibration, the nanobeam is prepared for the subsequent mechanical simulations, specifically free transverse vibration and bending analyses.

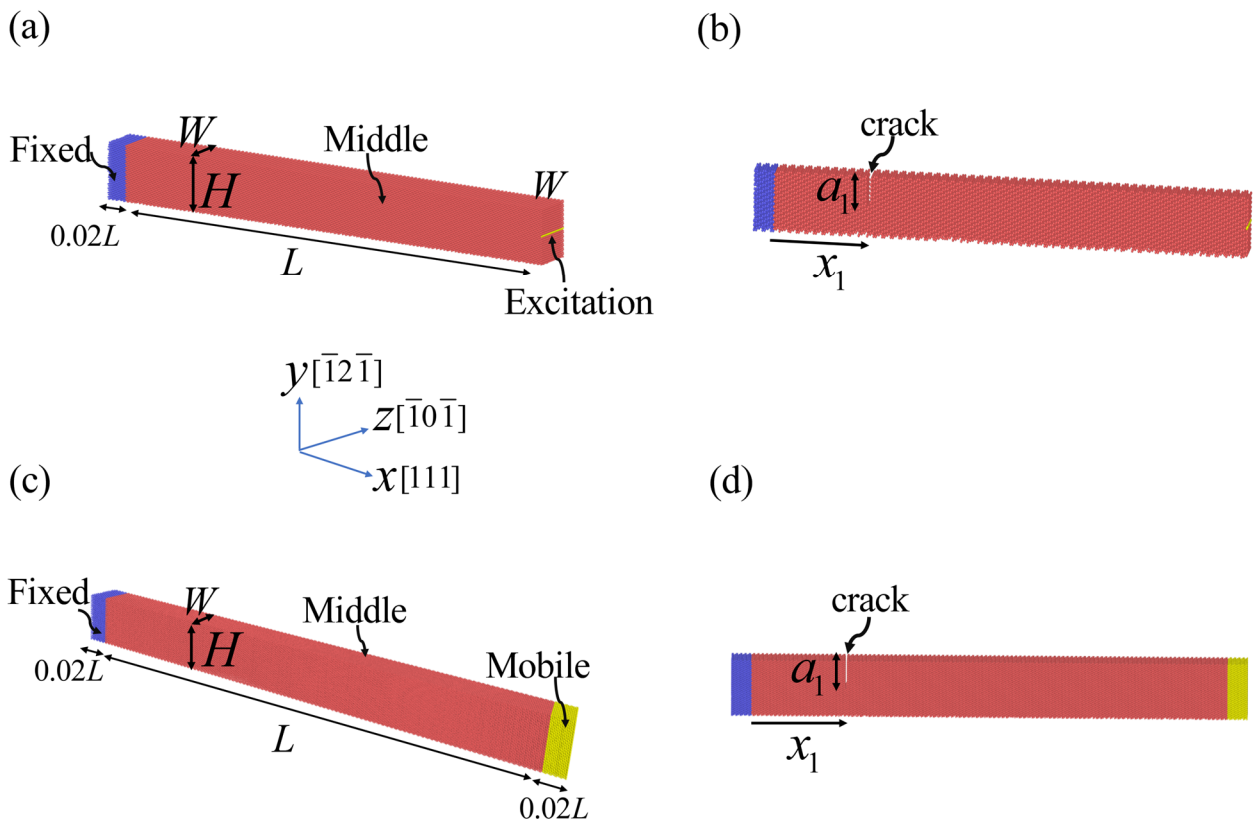

Fig. 2 Schematic of silicon nanobeams used in MD simulations. Cantilever beams for free transverse vibration: (a) intact and (b) with a crack of length a_1. Fixed–guided beams for bending simulations: (c) intact and (d) with a crack of length a_1. All nanobeams have a square cross-section with $W = H = L/12$.

3.1. MD simulation of free transverse vibration

The free transverse vibration behavior of the silicon cantilever nanobeams is investigated by first establishing a fixed–free configuration. As illustrated in Fig. 2(a), a region with length of $0.02L$ at the left end of the nanobeam (labeled “Fixed”) is fully constrained in all directions throughout the simulation, while the remainder of the nanobeam is allowed to deform.

After energy minimization and thermal equilibration, an excitation is applied to a small region near the free end along the y-axis to initiate vibration. Atoms inside this region are displaced at a prescribed constant velocity in the transverse (y) direction for a short duration to ensure that the

response remains within the elastic regime. This controlled motion generates an initial bent configuration and stores elastic energy in the beam, thereby establishing the initial conditions required for free vibration. During the excitation phase, atoms in the fixed region remain fully constrained, whereas atoms in the middle region are free to move and are maintained at 1 K using an NVT ensemble.

Once the desired initial deformation is achieved, the prescribed motion is removed, the thermostat is turned off, and the system transitions to the NVE ensemble. The beam then vibrates freely under the influence of its internal elastic forces. Throughout this stage, the average y-coordinate of atoms within the excitation region is recorded at each time step, providing a displacement signal from which the natural frequencies are extracted. Additional information, such as stress fields, potential energy, and kinetic energy, is also recorded for further evaluation of the vibrational response. Both intact and cracked nanobeams are examined. As shown in Fig. 2(b), cracks are introduced by deleting a single layer of atoms at the crack location. The free transverse vibration simulations are conducted for both intact and cracked beams of various lengths. Very long cracks are avoided to ensure that the crack surfaces remain open throughout the vibration process. The extracted natural frequencies for intact beams are used to calibrate the SDGE model parameters for silicon, while simulations of cracked beams quantify the variation of crack compliance with crack size and beam dimensions.

Fig. 3(a) illustrates how the first natural frequency of a cantilever intact nanobeam of length 104.28 nm is extracted from the MD simulation results by tracking the average y-coordinate of atoms within the excitation region over time t. The recorded vibration response is approximated using a sinusoidal function of the form

$$v(t) = A\sin(Bt + C) \qquad \Rightarrow \ \omega = 10^3 B \quad (\text{Giga rad/s}) \tag{11}$$

where A, B, and C are curve-fitting parameters, and displacement and time have the dimensions of Å and ps. The natural frequency of the nanobeam is then determined from the fitted parameter B, as $\omega = 10^3 B$, expressed in units of gigaradians per second (Giga rad/s). For the present case, the displacement profile is well captured by the function $17.66 \sin(6.06 \times 10^{-3} t + 4.239)$. From this fitting, the natural frequency of the nanobeam is determined to be $\omega = 6.06$ Gig rad/s.

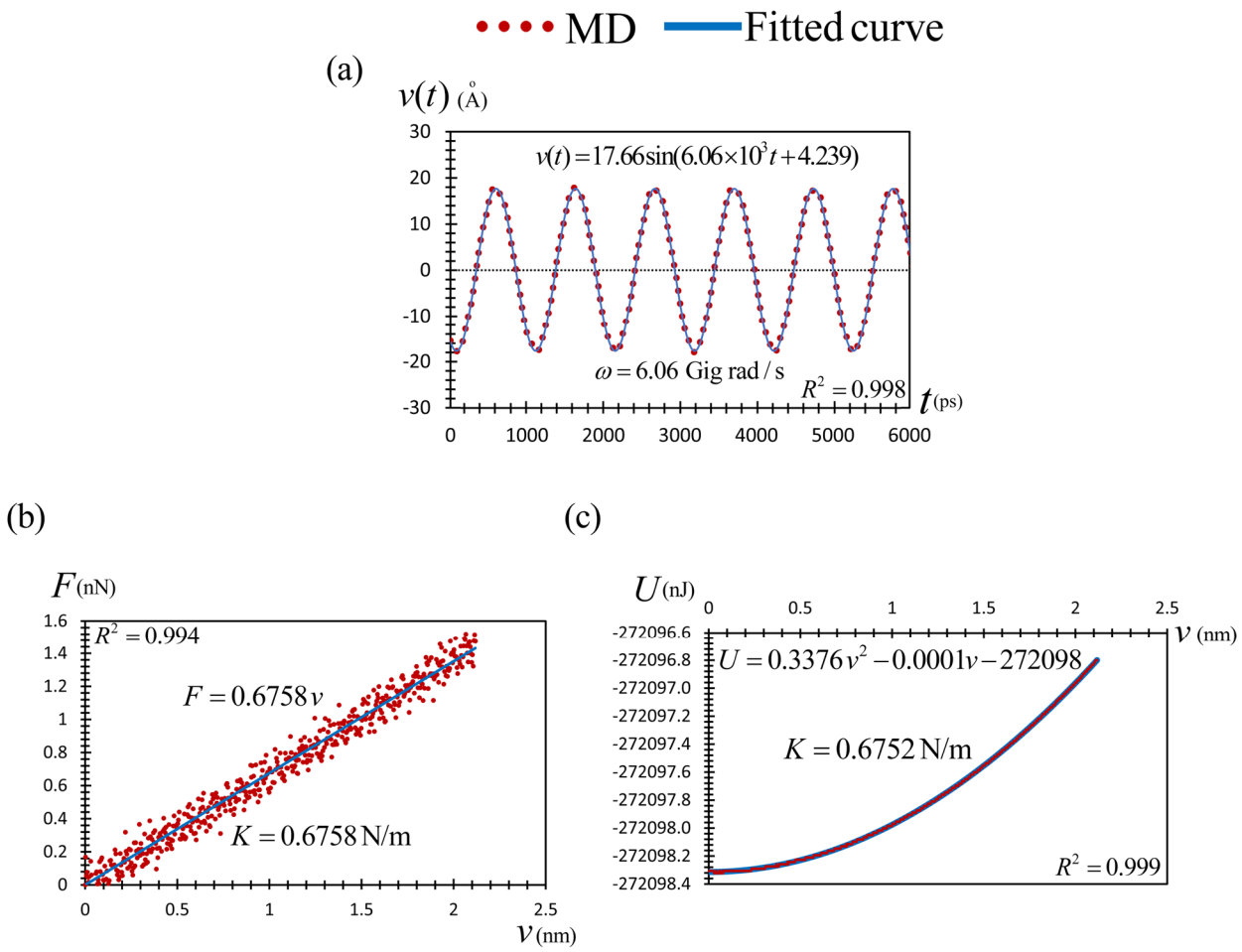

Fig. 3 (a) Derivation of the natural frequency of a cantilever nanobeam using MD results; and derivation of the bending stiffness of a fixed–guided nanobeam from MD results based on (b) the load–displacement curve and (c) the potential-energy–displacement curve. Both nanobeams have a length of $L = 104.28$ nm and an aspect ratio of $W = H = L/12$.

3.2. MD simulation of bending

Bending simulations are performed on nanobeams with a fixed–guided boundary conditions, where the beam is divided into three regions: Fixed, Middle, and Mobile, as shown in Fig. 2(c). The lengths of the fixed and mobile regions are each equal to $0.02L$.

Throughout the deformation process, the temperature is maintained at 1 K using the NVT ensemble. To simulate bending, atoms in the mobile region are displaced at a constant velocity

along the *y*-axis, while their movement in the other directions is constrained. This configuration models the bending of a fixed-guided nanobeam. To ensure a linear elastic response, the maximum displacement applied during the bending simulations is limited to 2.0% of the total beam length. Following each simulation, the results are processed to determine the bending stiffness of each nanobeam. This bending stiffness can be obtained either using the applied force at the guided end of the nanobeam or the potential energy of the middle region. In the first method, the bending stiffness is calculated as the slope of the load-displacement $(F - v)$ curve, as shown in Fig. 3(b). In the second method, as illustrated in Fig. 3(c), it is derived from the relationship between the potential energy (U) of the middle region and the displacement (v) at the guided end, expressed as follows:

$$K = \frac{d^2U}{dv^2} \tag{12}$$

Similar to the free transverse vibration simulations, the bending simulations are performed for both intact and cracked beams of various lengths. The bending stiffness values obtained from the MD simulations of intact nanobeams are used to calibrate the SDGE bending model parameters for silicon, while the simulations of cracked beams are employed to examine the size dependence of crack compliance.

4. Results and discussions

This section explores the existence of size effects on crack compliance in both free transverse vibration and bending problems of cracked silicon nanobeams at the nanoscale. First both SDGE models for bending and free transverse vibration are calibrated using data obtained from MD simulations. The calibrated SDGE models are then used to investigate the size dependence of crack compliance by comparing their predictions with the MD simulation results.

It should be noted that the Young's modulus of [1 1 1]-oriented bulk silicon is taken as $E = 142.85$ GPa, as predicted by SW potential [73]. Additionally, the density of silicon is $\rho = 2329\ {}^{kg}/_{m^3}$.

4.1. Calibration of SDGE models

Since the SDGE model contains three nonlocal parameters, it is necessary to determine their values for silicon with a [111] crystal orientation. The calibration is performed using MD simulation data for both bending and free transverse vibration of intact nanobeams with varying lengths and a fixed aspect ratio of $W = H = L/12$.

MD simulation results for the first natural frequencies (ω_{MD}) of intact cantilever silicon nanobeams, along with the corresponding predictions from the classical size-independent continuum model (ω_{Loc}) and their ratios, are summarized in Table 2. Similarly, Table 3 presents the MD-derived bending stiffness values (K_{MD}) for intact fixed-guided silicon nanobeams, together with the corresponding classical continuum predictions (K_{Loc}), and their ratios.

In addition, Fig. 4(a) and Fig. 4(b) illustrate the frequency ratios $(\frac{\omega_{\mathrm{MD}}}{\omega_{\mathrm{Loc}}})$ for cantilever nanobeams and bending stiffness ratios $(\frac{K_{\mathrm{MD}}}{K_{\mathrm{Loc}}})$ for fixed-guided nanobeams versus beam length. The curves clearly reveal pronounced size effects as both ratios are significantly less than one for short beams. For example, the frequency ratio is 0.844 and the bending stiffness ratio is 0.742 for the nanobeam with length of 26.07 nm. As the beam length increases, these size effects diminish, and the ratios approach unity. For the nanobeam with length of 182.48 nm, the frequency and bending stiffness ratios reach 0.981 and 0.997, respectively. These results indicate that size effects become negligible at lengths of this order, and the classical continuum models provide sufficiently accurate predictions.

Table 2

MD simulation results for the first natural frequencies (ω_{MD}) of intact cantilever nanobeams with varying lengths, along with the corresponding predictions from the classical size-independent continuum model (ω_{Loc}), and their ratios. The intact nanobeams have a square cross-section with dimensions $W = H = L/12$.

$\boldsymbol{L}$ (nm)	$\boldsymbol{\omega_{MD}}$ (Giga rad/s)	$\boldsymbol{\omega_{Loc}}$ (Giga rad/s)	$\frac{\boldsymbol{\omega_{MD}}}{\boldsymbol{\omega_{Loc}}}$
26.07	21.24	25.17	0.844
52.14	11.62	12.58	0.924
78.21	7.88	8.39	0.939
104.28	6.06	6.29	0.963
130.34	4.84	5.03	0.962
156.41	4.09	4.19	0.976
182.48	3.52	3.59	0.981

Table 3

MD simulation results for the bending stiffness (K_{MD}) of intact fixed-guided nanobeams with varying lengths, along with the corresponding predictions from the classical size-independent continuum model (K_{Loc}), and their ratio. The intact nanobeams have a square cross-section with dimensions $W = H = L/12$.

$\boldsymbol{L}$ (nm)	$\boldsymbol{K_{MD}}$ (N/m)	$\boldsymbol{K_{Loc}}$ (N/m)	$\frac{\boldsymbol{K_{MD}}}{\boldsymbol{K_{Loc}}}$
26.07	0.1305	0.1760	0.742
52.14	0.3102	0.3520	0.881
78.21	0.4779	0.5280	0.905
104.28	0.6752	0.7040	0.959
130.34	0.8374	0.8800	0.952
156.41	1.0270	1.0560	0.973
182.48	1.2282	1.2320	0.997

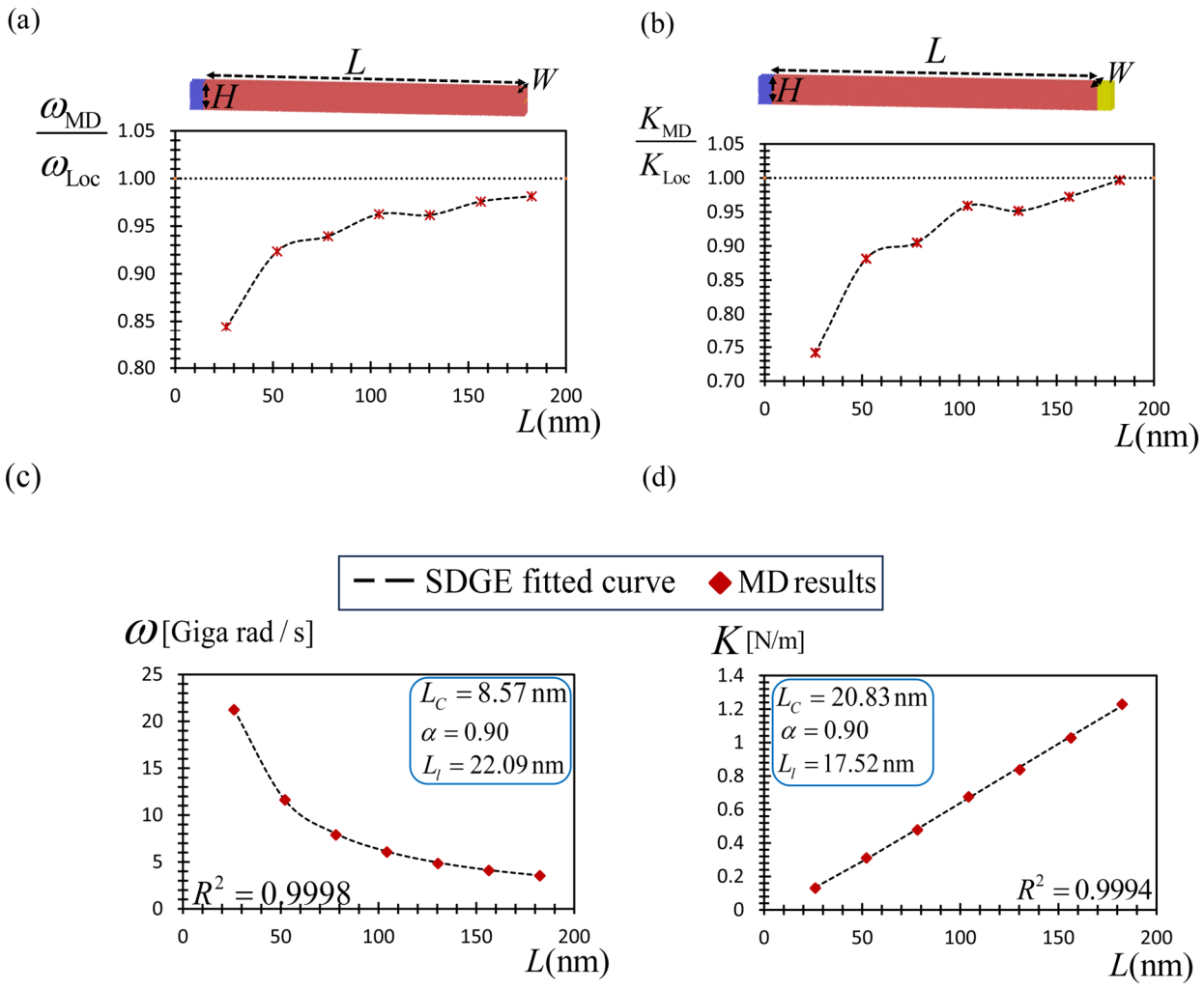

Fig. 4 (a) Frequency ratios ($\frac{\omega_{\mathrm{MD}}}{\omega_{\mathrm{Loc}}}$) for silicon cantilever nanobeams versus length, and (b) bending stiffness ratios ($\frac{K_{\mathrm{MD}}}{K_{\mathrm{Loc}}}$) for silicon fixed-guided nanobeams versus length; and calibration of the SDGE models using MD results for (c) free transverse vibration of silicon cantilever nanobeams, and (d) bending of silicon fixed-guided nanobeams. All nanobeams have a square cross-section with $W = H = L/12$.

The parameters of the SDGE models are determined using a nonlinear least-squares regression procedure [74]. The MD results for bending stiffness and natural frequencies are assumed to satisfy

$$\Upsilon_{\mathrm{MD}}(L_i) = \Upsilon_{\mathrm{SDGE}}(L_i; L_C, \alpha, L_l) + e_i \tag{13}$$

where e_i is the residual at each data point, defined as the difference between the SDGE model predictions and the corresponding MD results. Here, $\Upsilon = \omega$ for the vibration problem and $\Upsilon = K$ for the bending problem.

The parameter calibration problem is formulated as the minimization of a least-squares objective function $S(L_C, \alpha, L_l)$ as follows:

$$\min_{L_C,\alpha,L_l} S(L_C,\alpha,L_l) = \min_{L_C,\alpha,L_l} \sum_{i=1}^{N} e_i^2 = \sum_{i=1}^{N} \left[\Upsilon_{\mathrm{MD}}(L_i) - \Upsilon_{\mathrm{SDGE}}(L_i) \right]^2 \tag{14}$$

Because the SDGE predictions for bending stiffness and natural frequencies depend nonlinearly on the SDGE model parameters, the minimization problem is solved using an iterative procedure. At each iteration, the behavior of the nonlinear model in the vicinity of the current parameter estimates is used to guide the parameter update so as to reduce the least-squares objective function. The iterative process is repeated until successive iterations produce negligible changes in the parameter estimates and the least-squares objective function.

The accuracy of fit is quantified using the coefficient of determination R^2, defined as:

$$R^2 = 1 - \frac{SS_E}{SS_T} \tag{15}$$

where SS_E is the residual sum of squares and SS_T is the total sum of squares, given by:

$$\begin{aligned} SS_E &= \sum_{i=1}^{N} \left[\Upsilon_{\mathrm{SDGE}}(L_i) - \Upsilon_{\mathrm{MD}}(L_i) \right]^2 \\ SS_T &= \sum_{i=1}^{N} \left[\Upsilon_{\mathrm{MD}}(L_i) - \overline{\Upsilon}_{\mathrm{MD}} \right]^2 \end{aligned} \tag{16}$$

Here, $\overline{\Upsilon}_{MD}$ denotes the average of the MD results for bending stiffness or natural frequencies.

A comparison between MD results and the calibrated SDGE model predictions are illustrated in Fig. 4(c) and Fig. 4(d) respectively. The resulting calibrated nonlocal parameter values are summarized in Table 4.

Table 4

Calibrated nonlocal parameters of the SDGE bending and vibration models based on MD simulation data.

Problem	$\boldsymbol{L_C}$ (nm)	$\boldsymbol{\alpha}$	$\boldsymbol{L_l}$ (nm)	$\mathbf{R^2}$
Vibration	8.57	0.90	22.09	0.9998
Bending	20.83	0.90	17.52	0.9994

4.2. Size dependence of crack compliance

Using the calibrated nonlocal parameters, the SDGE vibration model is applied to examine the influence of size effects on crack compliance in free transverse vibration of cantilever nanobeams containing an edge crack. The natural frequencies of cracked nanobeams with varying lengths and a fixed aspect ratio of $W = H = L/12$ are computed using the calibrated SDGE model and compared with the corresponding MD simulation results to assess whether the crack compliance exhibits size dependency.

It is important to note that, at the cracked cross-section, the crack compliance of each rotational spring C_θ is evaluated using the closed-form expressions provided in Eq. (6). This expression, which is based on classical fracture mechanics within the framework of local elasticity, does not include any size effects. Thus, any deviation between the results of MD simulations and the calibrated SDGE vibration model for cracked nanobeams reflects the size effect on the crack compliance that is not captured by the classical expression in Eq. (6).

For the MD simulations of cracked nanobeams, the same overall configuration used for the intact beams is used. Silicon cantilever nanobeams with a single edge crack located at $x_1 = 0.2\,L$ are considered, with crack lengths of $a_1 = 0.25\,H$ and $a_1 = 0.5\,H$.

Fig. 5(a) illustrates the ratios of the MD-predicted natural frequencies to the SDGE predictions for cracked nanobeams. For shorter beams and crack length of $a_1 = 0.5\,H$, the MD-predicted frequencies are significantly lower than the SDGE results, consistent with the size-dependent softening behavior previously observed in intact beams. In this case, however, the discrepancy arises from a pronounced size effect in the crack compliance. For example, the ratio is 0.795 for a nanocantilever of length 26.07 nm. As the nanobeam length increases, the size effect on crack compliance diminishes, and the MD results converge toward the calibrated SDGE predictions, with the ratio reaching 0.964 for a length of 182.28 nm.

For nanobeams containing a crack of length $a_1 = 0.25\,H$, the size effect on crack compliance is less pronounced than that for $a_1 = 0.5\,H$; nevertheless, the same trend is observed. The ratio increases from 0.918 for a nanocantilever of length 26.07 nm to 0.980 for a nanobeam of length 182.28 nm.

These observations demonstrate that crack compliance in nanobeams is size-dependent and cannot be accurately captured using classical formulas derived from local fracture mechanics, Eq. (6). The MD simulations reveal that cracks introduce greater flexibility at small scales than predicted by size-independent models. As the nanobeam length grows, these effects become less dominant, and the classical expression becomes effectively valid in the limit of large lengths.

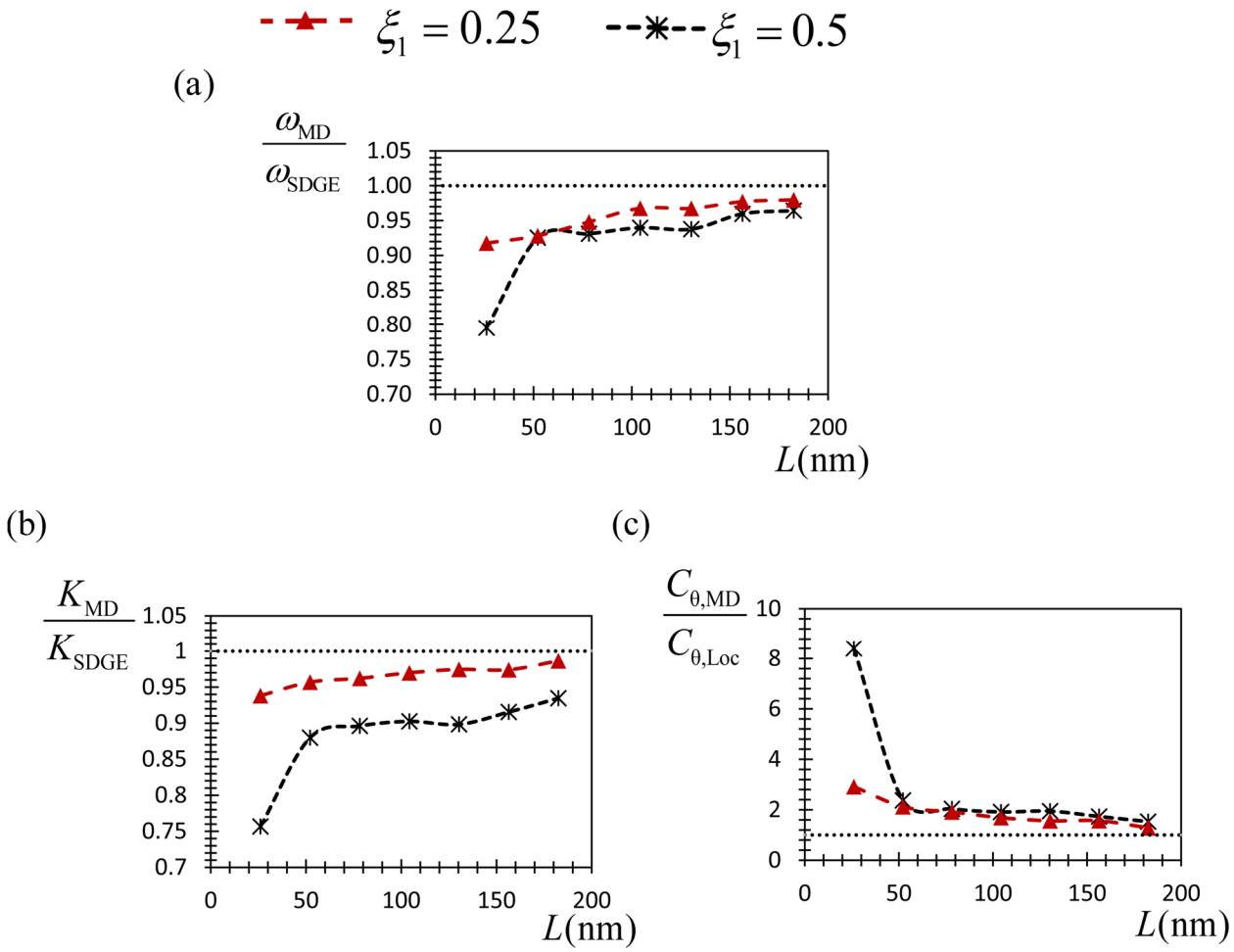

Fig. 5 (a) Ratios of natural frequencies from MD simulations (ω_{MD}) to those predicted by the calibrated SDGE model (ω_{SDGE}) versus silicon cantilever length. (b) Ratios of bending stiffness from MD simulations (K_{MD}) to calibrated SDGE predictions (K_{SDGE}) versus fixed–guided nanobeam length. (c) Ratio of crack compliances from MD simulations ($C_{\theta,MD}$) to the predictions of size-independent model [69] ($C_{\theta,Loc}$) versus fixed–guided nanobeam length. All nanobeams have a square cross-section with dimensions $W = H = L/12$, and contain a single edge crack at $x_1 = 0.2L$ with crack length of $a_1 = 0.25H$ and $0.5H$.

In addition, the calibrated SDGE bending model is employed to predict the bending stiffness of fixed–guided cracked nanobeams with varying lengths, and the results are compared with MD simulations to assess the size dependence of crack compliance.

Fixed–guided silicon nanobeams containing a single edge crack located at $x_1 = 0.2\,L$ are analyzed for two crack lengths, $a_1 = 0.25\,H$ and $a_1 = 0.5\,H$. The comparative results of MD simulations

and the calibrated SDGE bending model for cracked silicon nanobeams are presented in Fig. 5(b). The comparison involves calculating the ratios of bending stiffness values obtained from MD simulations (K_{MD}) to those predicted by the calibrated SDGE model (K_{SDGE}).

As shown in Fig. 5(b), a significant discrepancy is observed between the MD-derived bending stiffness values (K_{MD}) and those predicted by the calibrated SDGE model (K_{MD}) for the nanobeams with a crack length $a_1 = 0.5\,H$, particularly for shorter nanobeams. For example, for a nanobeam with $L = 26.07$ nm, the ratio $\frac{K_{\mathrm{MD}}}{K_{\mathrm{SDGE}}}$ is 0.756, indicating a pronounced size effect associated with crack compliance. Consistent with the trends observed in the vibration analysis, this discrepancy decreases as the nanobeam length increases, and the ratio $\frac{K_{\mathrm{MD}}}{K_{\mathrm{SDGE}}}$ gradually approaches unity, demonstrating that the size effect on crack compliance diminishes for longer beams.

For nanobeams containing a shorter crack of $a_1 = 0.25\,H$, the size effect is less pronounced. In this case, the ratio $\frac{K_{\mathrm{MD}}}{K_{\mathrm{SDGE}}}$ is 0.938 for $L = 26.07$ nm, reflecting reduced size sensitivity due to the smaller crack length. Nevertheless, the same trend is observed, with the ratio approaching unity as the nanobeam length increases, indicating the gradual disappearance of size effects on crack compliance.

Since a size-independent formula is used to calculate crack compliance (C_θ) within the SDGE model framework, the discrepancy between the MD simulation results and those obtained from the calibrated SDGE bending model is attributed to the presence of size effect in crack compliance. Notably, as the nanobeam length increases, the size effect progressively disappears and the bending stiffness values converge to those of the corresponding size-independent local model.

Moreover, the MD simulation results are used to determine the crack compliance values ($C_{\theta,\mathrm{MD}}$), which are compared with those obtained from the size-independent formulation ($C_{\theta,\mathrm{Loc}}$) given in Eq.(6). This is achieved by substituting the bending stiffness values derived from MD simulations into the SDGE model and calculating the corresponding crack compliance that results in this bending stiffness. Similar to the trend observed in the curve of bending stiffness ratios, Fig. 5(c) clearly shows that the size effect on crack compliance is significantly more pronounced in shorter nanobeams. For example, for the nanobeam with $L = 26.07$ nm and a crack of length $a_1 = 0.5\,H$,

the ratio $\frac{C_{\theta,\mathrm{MD}}}{C_{\theta,\mathrm{Loc}}}$ is 8.404. This size effect diminishes as the crack length decreases; for the same nanobeam with $a_1 = 0.25\,H$, the ratio is reduced to 2.916.

Furthermore, as the nanobeam length increases, the crack compliance values obtained from MD simulations for both crack lengths gradually converge toward those predicted by the size-independent formulation in Eq.(6), indicating the progressive disappearance of size effects in longer nanobeams.

The bending analysis further confirms that crack compliance is size-dependent which not captured by classical local models. At small scales, MD simulations reveal greater flexibility than predicted by size-independent models. With increasing beam length, the influence of these nanoscale effects on crack compliance diminishes, and the classical formulation becomes progressively more accurate.

5. Conclusions

This study examined the influence of size effects on crack compliance in cracked silicon nanobeams by integrating MD simulations with nonlocal elasticity theory. Both bending and free transverse vibration analyses were conducted on nanobeams containing single edge crack. The nonlocal parameters for static and dynamic responses were determined based on MD results for intact nanobeams. These calibrated models were then applied to evaluate the crack compliance of nanobeams across a wide range of lengths.

The results demonstrated a pronounced size effect on crack compliance, especially in short nanobeams. MD simulations revealed that classical size-independent formulas significantly underestimate the crack-induced flexibility at the nanoscale. As the nanobeam length increases, the discrepancy between MD predictions and classical models diminishes, and crack compliance converges toward values consistent with large-scale continuum theory.

Overall, the findings show that classical crack compliance models are inadequate for nanoscale applications. Accurate and reliable crack detection in nanostructures requires models that explicitly incorporate size-dependent effects at cracked cross-sections. Such enhanced models are essential for advancing the structural health monitoring and design of nanoscale devices, including MEMS and NEMS.

Funding

The financial support provided by the National Science Centre (NCN) in Poland through the grant agreement No: UMO-2022/47/D/ST8/01348, is gratefully acknowledged.

Acknowledgment

The authors gratefully acknowledge Polish high-performance computing infrastructure PLGrid (HPC Centers: WCSS, ACK Cyfronet AGH) for providing computer facilities and support within computational grant no. PLG/2025/018166.

Declaration of interests

The authors declare that they have no known competing financial interests or personal relationships that could have appeared to influence the work reported in this paper.

Appendix A

The integral representation of the constitutive law in Eq.(7) is mathematically equivalent to the following differential equation for sub-beam k [75]:

$$\chi_k - L_C^2 \frac{d^2\chi_k}{dx^2} = C M_k - C(\alpha L_C^2 + L_l^2) \frac{d^2 M_k}{dx^2} \tag{A.1}$$

for k = 1 and 2.

The transformation of the integral form of the constitutive law in Eq.(7) into the differential form in Eq.(A.1) yields the following constitutive boundary and continuity conditions [75]:

$$L_C^2 \frac{d^3 v_1(x,t)}{dx^3} - L_C \frac{d^2 v_1(x,t)}{dx^2} + C\alpha L_C M_1(x,t) - C(\alpha L_C^2 + L_l^2) \frac{dM_1(x,t)}{dx} = 0 \qquad \text{at } x = 0 \tag{A.2}$$

(A.3)

$$L_C^2\frac{d^3v_2(x,t)}{dx^3}+L_C\frac{d^2v_2(x,t)}{dx^2}-C\alpha L_C M_2(x,t)-C(\alpha L_C^2+L_l^2)\frac{dM_2(x,t)}{dx}=0 \qquad \text{at } x=L$$

$$\begin{aligned}&L_C^2\frac{d^3v_1(x,t)}{dx^3}+L_C\frac{d^2v_1(x,t)}{dx^2}-C\alpha L_C M_1(x,t)-C\alpha L_C^2\frac{dM_1(x,t)}{dx}\\&-C(1-\alpha)\left[\int_{x_1}^{x_2}e^{\frac{x-\zeta}{L_C}}M_2(\zeta,t)\,d\zeta\right] \qquad \text{at } x=x_1\\&+CL_l^2\left[\frac{d}{dx}\int_{x}^{x_1}e^{\frac{x-\zeta}{L_C}}\frac{dM_1(\zeta,t)}{d\zeta}d\zeta+\frac{d}{dx}\int_{x_1}^{x_2}e^{\frac{x-\zeta}{L_C}}\frac{dM_2(\zeta,t)}{d\zeta}d\zeta\right]=0\end{aligned} \tag{A.4}$$

$$\begin{aligned}&L_C^2\frac{d^3v_2(x,t)}{dx^3}-L_C\frac{d^2v_2(x,t)}{dx^2}+C\alpha L_C M_2(x,t)-C\alpha L_C^2\frac{dM_2(x,t)}{dx}\\&+C(1-\alpha)\left[\int_{0}^{x_1}e^{-\frac{x-\zeta}{L_C}}M_1(\zeta,t)\,d\zeta\right] \qquad \text{at } x=x_1\\&-CL_l^2\left[\frac{d}{dx}\int_{0}^{x_1}e^{-\frac{x-\zeta}{L_C}}\frac{dM_1(\zeta,t)}{d\zeta}d\zeta+\frac{d}{dx}\int_{x_1}^{x}e^{-\frac{x-\zeta}{L_C}}\frac{dM_2(\zeta,t)}{d\zeta}d\zeta\right]=0\end{aligned} \tag{A.5}$$

According to the Euler-Bernoulli beam theory, the relationship between transverse displacement $v(x,t)$, cross-section rotation $\theta(x,t)$ and the elastic curvature of the beam $\chi(x,t)$ are as follows:

$$\theta_k(x,t)=\frac{\partial v_k(x,t)}{\partial x} \tag{A.6}$$

$$\chi_k(x,t)=\frac{\partial\theta_k(x,t)}{\partial x} \tag{A.7}$$

Accordingly:

$$\chi_k(x,t)=\frac{\partial^2 v_k(x,t)}{\partial x^2} \tag{A.8}$$

for k = 1 and 2.

The dynamic equilibrium equations for the free transverse vibration of sub-beam k based on the Euler-Bernoulli beam model are:

$$\frac{\partial Q_k(x,t)}{\partial x}=-I_0\,\ddot{v}_k(x,t) \tag{A.9}$$

$$\frac{\partial M_k(x,t)}{\partial x}-Q_k(x,t)=I_2\,\ddot{\theta}_k(x,t) \tag{A.10}$$

Where Q and M are shear force and bending moment, respectively. In addition, $\ddot{v}_k$ and $\ddot{\theta}_k$ represent the second derivative of v_k and θ_k with respect to time.

Substituting Eq.(A.10) into Eq. (A.9) gives:

$$\frac{\partial^2 M_k(x,t)}{\partial x^2}-I_2\frac{\partial^2\ddot{v}_k(x,t)}{\partial x^2}+I_0\ddot{v}_k(x,t)=0 \tag{A.11}$$

By incorporating Eq.(A.1) into the Euler–Bernoulli beam theory and using Eq.(A.11), the governing differential equation for the dynamic behavior of the nanobeam is obtained as follows:

$$L_C^2 \frac{d^6 v_k}{dx^6} - \frac{d^4 v_k}{dx^4} - C(\alpha L_C^2 + L_l^2)\frac{d^4 \ddot{v}_k}{dx^4} + \left(CI_2 + CI_0(\alpha L_C^2 + L_l^2)\right)\frac{d^2 \ddot{v}_k}{dx^2} - CI_0 \ddot{v}_k = 0 \tag{A.12}$$

for k = 1 and 2.

Additionally, the equations for the bending moment (M) and shear force (Q) are derived as follows:

$$\begin{aligned} M_k &= \frac{1}{C}\left(\frac{d^2 v_k}{dx^2} - L_C^2 \frac{d^4 v_k}{dx^4}\right) + I_2(\alpha L_C^2 + L_l^2)\frac{d^2 \ddot{v}_k}{dx^2} - I_0(\alpha L_C^2 + L_l^2)\ddot{v}_k \\ Q_k &= \frac{1}{C}\left(\frac{d^3 v_k}{dx^3} - L_C^2 \frac{d^5 v_k}{dx^5}\right) + I_2(\alpha L_C^2 + L_l^2)\frac{d^3 \ddot{v}_k}{dx^3} - \left(I_0(\alpha L_C^2 + L_l^2) - I_2\right)\frac{d\ddot{v}_k}{dx} \end{aligned} \tag{A.13}$$

To solve the governing differential equations in (A.12) for the free transverse vibration of an Euler-Bernoulli nanobeam, the displacement function is separated into a harmonic time-dependent component and a spatial function. Assuming a harmonic response, the displacements can be expressed as:

$$\begin{aligned} v_k(x,t) &= e^{i\omega t} V_k(x) \\ \theta_k(x,t) &= e^{i\omega t}\, \Phi_k(x) \end{aligned} \tag{A.14}$$

where ω is the frequency.

Substituting Eq.(A.14) into the governing differential equation (A.12), results in the following spatial form of governing equation:

$$L_C^2 \frac{d^6 v_k}{dx^6} - \frac{d^4 v_k}{dx^4} + C(\alpha L_C^2 + L_l^2)\omega^2 \frac{d^4 V_k}{dx^4} - \left(CI_2 + CI_0(\alpha L_C^2 + L_l^2)\right)\omega^2 \frac{d^2 V_k}{dx^2} + CI_0 \omega^2 V_k = 0 \tag{A.15}$$

for k = 1 and 2.

Solving the governing differential equation (A.15) for free transverse vibrations of a cantilever nanobeam requires 12 boundary and continuity conditions. Among these, two are the constitutive

boundary conditions given in equations (A.2) and (A.3), and two are the constitutive continuity conditions specified in equations (A.4) and (A.5).

In addition, four variationally consistent continuity conditions at each cracked cross-section are given by:

$$\begin{aligned} &M_1 = M_2 \\ &Q_1 = Q_2 \qquad\qquad \text{at } x = x_1 \\ &V_1 = V_2 \\ &\frac{dV_2}{dx} - \frac{dV_1}{dx} = C_\theta M_1 \end{aligned} \tag{A.16}$$

Finally, four variationally consistent boundary conditions for a cantilever beam are expressed as

$$\begin{aligned} &V_1 = 0 \qquad\qquad \text{at } x = 0 \\ &\frac{dV_1}{dx} = 0 \qquad\qquad \text{at } x = 0 \\ &Q_2 = 0 \qquad\qquad \text{at } x = L \\ &M_2 = 0 \qquad\qquad \text{at } x = L \end{aligned} \tag{A.17}$$

Further details on the numerical solution procedure for analyzing the free transverse vibration of small-scale beams using the SDGE model can be found in [70].

For the bending problem, the solution is obtained directly from the dynamic formulation by removing all time-dependent terms. Applying this reduction to Eq. (A.12) yields the governing differential equation for the static bending response of the nanobeam, expressed as:

$$L_C^2 \frac{d^6 v_k}{dx^6} - \frac{d^4 v_k}{dx^4} = 0 \tag{A.18}$$

for k = 1 and 2. Similar to the free transverse vibration problem, solving the differential equation (A.18) governing the bending behavior of the nanobeam requires 12 boundary and continuity conditions. Among these conditions, two are the constitutive boundary conditions given in Eqs.

(A.2) and (A.3), and two are the continuity conditions expressed in equations (A.4) and (A.5). In addition, four variationally consistent continuity conditions at each cracked cross-section are provided in Eq. (A.16).

However, because the bending analysis considers a fixed–guided nanobeam, the corresponding variationally consistent boundary conditions are given below:

$$\begin{aligned} &v_1 = 0 && \text{at } x = 0 \\ &\frac{dv_1}{dx} = 0 && \text{at } x = 0 \\ &Q_2 = F && \text{at } x = L \\ &\frac{dv_2}{dx} = 0 && \text{at } x = L \end{aligned} \tag{A.19}$$

It should be noted that the bending stiffness of the fixed–guided nanobeam is defined as:

$$K = \frac{F}{v_2(x = L)} \tag{A.20}$$

References

[1] B. Bhushan, Introduction to Nanotechnology, in: B. Bhushan (Ed.), Springer Handbook of Nanotechnology, Springer, Berlin, Heidelberg, 2017: pp. 1–19. https://doi.org/10.1007/978-3-662-54357-3_1.

[2] Jeremy J. Ramsden, Nanotechnology: An Introduction, William Andrew (2016). https://doi.org/10.1016/C2014-0-03912-3.

[3] B. Bhushan, Nanotribology and nanomechanics of MEMS/NEMS and BioMEMS/BioNEMS materials and devices, Microelectronic Engineering 84 (2007) 387–412. https://doi.org/10.1016/j.mee.2006.10.059.

[4] R. Kumar, R. Singh, D. Hui, L. Feo, F. Fraternali, Graphene as biomedical sensing element: State of art review and potential engineering applications, Composites Part B: Engineering 134 (2018) 193–206. https://doi.org/10.1016/j.compositesb.2017.09.049.

[5] K.L. Ekinci, M.L. Roukes, Nanoelectromechanical systems, Review of Scientific Instruments 76 (2005) 061101. https://doi.org/10.1063/1.1927327.

[6] V.S. Chandel, G. Wang, M. Talha, Advances in modelling and analysis of nano structures: a review, Nanotechnology Reviews 9 (2020) 230–258. https://doi.org/10.1515/ntrev-2020-0020.

[7] Z. Chen, T. Wang, Q. Jia, J. Yang, Q. Yuan, Y. Zhu, F. Yang, A Novel Lamé Mode RF-MEMS resonator with high quality factor, International Journal of Mechanical Sciences 204 (2021) 106484. https://doi.org/10.1016/j.ijmecsci.2021.106484.

[8] A.M. Alneamy, H.M. Ouakad, Inertia mass bio-sensors based on snap-through phenomena in electrostatic MEMS shallow arch resonators, International Journal of Mechanical Sciences 238 (2023) 107825. https://doi.org/10.1016/j.ijmecsci.2022.107825.

[9] V.C. Meesala, M.R. Hajj, E. Abdel-Rahman, Bifurcation-based MEMS mass sensors, International Journal of Mechanical Sciences 180 (2020) 105705. https://doi.org/10.1016/j.ijmecsci.2020.105705.

[10] N.V. Lavrik, M.J. Sepaniak, P.G. Datskos, Cantilever transducers as a platform for chemical and biological sensors, Review of Scientific Instruments 75 (2004) 2229–2253. https://doi.org/10.1063/1.1763252.

[11] D. Acquaviva, A. Arun, R. Smajda, D. Grogg, A. Magrez, T. Skotnicki, A.M. Ionescu, Micro-Electro-Mechanical Switch Based on Suspended Horizontal Dense Mat of CNTs by FIB Nanomanipulation, Procedia Chemistry 1 (2009) 1411–1414. https://doi.org/10.1016/j.proche.2009.07.352.

[12] C. Chen, S. Lee, V.V. Deshpande, G.-H. Lee, M. Lekas, K. Shepard, J. Hone, Graphene mechanical oscillators with tunable frequency, Nature Nanotech 8 (2013) 923–927. https://doi.org/10.1038/nnano.2013.232.

[13] A.W. Knoll, D. Grogg, M. Despont, U. Duerig, Fundamental scaling properties of electro-mechanical switches, New J. Phys. 14 (2012) 123007. https://doi.org/10.1088/1367-2630/14/12/123007.

[14] D. Grogg, U. Drechsler, A. Knoll, U. Duerig, Y. Pu, C. Hagleitner, M. Despont, Curved in-plane electromechanical relay for low power logic applications, J. Micromech. Microeng. 23 (2013) 025024. https://doi.org/10.1088/0960-1317/23/2/025024.

[15] J.D. Zook, D.W. Burns, H. Guckel, J.J. Sniegowski, R.L. Engelstad, Z. Feng, Characteristics of polysilicon resonant microbeams, Sensors and Actuators A: Physical 35 (1992) 51–59. https://doi.org/10.1016/0924-4247(92)87007-4.

[16] J. Lim, H. Kim, T.N. Jackson, K. Choi, D. Kenny, An ultra-compact and low-power oven-controlled crystal oscillator design for precision timing applications, IEEE Transactions on Ultrasonics, Ferroelectrics, and Frequency Control 57 (2010) 1906–1914. https://doi.org/10.1109/TUFFC.2010.1638.

[17] L.G. Villanueva, R.B. Karabalin, M.H. Matheny, E. Kenig, M.C. Cross, M.L. Roukes, A Nanoscale Parametric Feedback Oscillator, ACS Publications (2011). https://doi.org/10.1021/nl2031162.

[18] X.L. Feng, C.J. White, A. Hajimiri, M.L. Roukes, A self-sustaining ultrahigh-frequency nanoelectromechanical oscillator, Nature Nanotech 3 (2008) 342–346. https://doi.org/10.1038/nnano.2008.125.

[19] M.S. Hanay, S. Kelber, A.K. Naik, D. Chi, S. Hentz, E.C. Bullard, E. Colinet, L. Duraffourg, M.L. Roukes, Single-protein nanomechanical mass spectrometry in real time, Nature Nanotech 7 (2012) 602–608. https://doi.org/10.1038/nnano.2012.119.

[20] J. Chaste, A. Eichler, J. Moser, G. Ceballos, R. Rurali, A. Bachtold, A nanomechanical mass sensor with yoctogram resolution, Nature Nanotech 7 (2012) 301–304. https://doi.org/10.1038/nnano.2012.42.

[21] A. Boisen, S. Dohn, S.S. Keller, S. Schmid, M. Tenje, Cantilever-like micromechanical sensors, Rep. Prog. Phys. 74 (2011) 036101. https://doi.org/10.1088/0034-4885/74/3/036101.

[22] J.L. Arlett, E.B. Myers, M.L. Roukes, Comparative advantages of mechanical biosensors, Nature Nanotech 6 (2011) 203–215. https://doi.org/10.1038/nnano.2011.44.

[23] J. Moser, J. Güttinger, A. Eichler, M.J. Esplandiu, D.E. Liu, M.I. Dykman, A. Bachtold, Ultrasensitive force detection with a nanotube mechanical resonator, Nature Nanotech 8 (2013) 493–496. https://doi.org/10.1038/nnano.2013.97.

[24] T. Larsen, S. Schmid, L.G. Villanueva, A. Boisen, Photothermal Analysis of Individual Nanoparticulate Samples Using Micromechanical Resonators, ACS Publications (2013). https://doi.org/10.1021/nn402057f.

[25] X.C. Zhang, E.B. Myers, J.E. Sader, M.L. Roukes, Nanomechanical Torsional Resonators for Frequency-Shift Infrared Thermal Sensing, ACS Publications (2013). https://doi.org/10.1021/nl304687p.

[26] J. Lee, Identification of multiple cracks in a beam using vibration amplitudes, Journal of Sound and Vibration 326 (2009) 205–212. https://doi.org/10.1016/j.jsv.2009.04.042.

[27] A.C. Altunışık, F.Y. Okur, S. Karaca, V. Kahya, Vibration-based damage detection in beam structures with multiple cracks: modal curvature vs. modal flexibility methods, Nondestructive Testing and Evaluation 34 (2019) 33–53. https://doi.org/10.1080/10589759.2018.1518445.

[28] Ş.D. Akbaş, Wave Propagation Analysis of Edge Cracked Circular Beams under Impact Force, PLOS ONE 9 (2014) e100496. https://doi.org/10.1371/journal.pone.0100496.

[29] S. He, C.-T. Ng, Guided wave-based identification of multiple cracks in beams using a Bayesian approach, Mechanical Systems and Signal Processing 84 (2017) 324–345. https://doi.org/10.1016/j.ymssp.2016.07.013.

[30] S. Caddemi, A. Morassi, Crack detection in elastic beams by static measurements, International Journal of Solids and Structures 44 (2007) 5301–5315. https://doi.org/10.1016/j.ijsolstr.2006.12.033.

[31] S.S. Naik, Crack Detection in Pipes Using Static Deflection Measurements, J. Inst. Eng. India Ser. C 93 (2012) 209–215. https://doi.org/10.1007/s40032-012-0027-z.

[32] Y. Narkis, Identification of Crack Location in Vibrating Simply Supported Beams, Journal of Sound and Vibration 172 (1994) 549–558. https://doi.org/10.1006/jsvi.1994.1195.

[33] S.P. Lele, S.K. Maiti, Modelling of transverse vibration of short beams for crack detection and measurement of crack extension, Journal of Sound and Vibration 257 (2002) 559–583. https://doi.org/10.1006/jsvi.2002.5059.

[34] J. Wang, P. Qiao, Vibration of beams with arbitrary discontinuities and boundary conditions, Journal of Sound and Vibration 308 (2007) 12–27. https://doi.org/10.1016/j.jsv.2007.06.071.

[35] S. Hadian Jazi, M. Hadian, K. Torabi, An exact closed-form explicit solution of free transverse vibration for non-uniform multi-cracked beam, Journal of Sound and Vibration 570 (2024) 117986. https://doi.org/10.1016/j.jsv.2023.117986.

[36] F. Cannizzaro, I. Fiore, A. Greco, S. Caddemi, I. Caliò, Eigenproperties of multi-cracked circular arches, Journal of Sound and Vibration 543 (2023) 117365. https://doi.org/10.1016/j.jsv.2022.117365.

[37] A.C. Eringen, D.G.B. Edelen, On nonlocal elasticity, International Journal of Engineering Science 10 (1972) 233–248. https://doi.org/10.1016/0020-7225(72)90039-0.

[38] S.C. Pradhan, J.K. Phadikar, Nonlocal elasticity theory for vibration of nanoplates, Journal of Sound and Vibration 325 (2009) 206–223. https://doi.org/10.1016/j.jsv.2009.03.007.

[39] N. Challamel, S. El-Borgi, M. Trabelssi, J.N. Reddy, Free vibration response of micromorphic Timoshenko beams, Journal of Sound and Vibration 591 (2024) 118602. https://doi.org/10.1016/j.jsv.2024.118602.

[40] L. Tong, Y. Yu, W. Hu, Y. Shi, C. Xu, On wave propagation characteristics in fluid saturated porous materials by a nonlocal Biot theory, Journal of Sound and Vibration 379 (2016) 106–118. https://doi.org/10.1016/j.jsv.2016.05.042.

[41] J.N. Reddy, Nonlocal theories for bending, buckling and vibration of beams, International Journal of Engineering Science 45 (2007) 288–307. https://doi.org/10.1016/j.ijengsci.2007.04.004.

[42] C.W. Lim, G. Zhang, J.N. Reddy, A higher-order nonlocal elasticity and strain gradient theory and its applications in wave propagation, Journal of the Mechanics and Physics of Solids 78 (2015) 298–313. https://doi.org/10.1016/j.jmps.2015.02.001.

[43] G. Lovisi, Application of the surface stress-driven nonlocal theory of elasticity for the study of the bending response of FG cracked nanobeams, Composite Structures 324 (2023) 117549. https://doi.org/10.1016/j.compstruct.2023.117549.

[44] S.D. Akbas, Bending of a cracked functionally graded nanobeam, Advances in Nano Research 6 (2018) 219–242. https://doi.org/10.12989/anr.2018.6.3.219.

[45] M. Soltanpour, M. Ghadiri, A. Yazdi, M. Safi, Free transverse vibration analysis of size dependent Timoshenko FG cracked nanobeams resting on elastic medium, Microsyst Technol 23 (2017) 1813–1830. https://doi.org/10.1007/s00542-016-2983-3.

[46] J. Loya, J. López-Puente, R. Zaera, J. Fernández-Sáez, Free transverse vibrations of cracked nanobeams using a nonlocal elasticity model, Journal of Applied Physics 105 (2009) 044309. https://doi.org/10.1063/1.3068370.

[47] I. Esen, C. Özarpa, M.A. Eltaher, Free vibration of a cracked FG microbeam embedded in an elastic matrix and exposed to magnetic field in a thermal environment, Composite Structures 261 (2021) 113552. https://doi.org/10.1016/j.compstruct.2021.113552.

[48] S. Dastjerdi, M. Abbasi, A vibration analysis of a cracked micro-cantilever in an atomic force microscope by using transfer matrix method, Ultramicroscopy 196 (2019) 33–39. https://doi.org/10.1016/j.ultramic.2018.09.014.

[49] H. Darban, R. Luciano, M. Basista, Effects of multiple edge cracks, shear force, elastic foundation, and boundary conditions on bucking of small-scale pillars, International Journal of Damage Mechanics 33 (2024) 247–268. https://doi.org/10.1177/10567895231215558.

[50] R. Barretta, F. Marotti de Sciarra, Variational nonlocal gradient elasticity for nano-beams, International Journal of Engineering Science 143 (2019) 73–91. https://doi.org/10.1016/j.ijengsci.2019.06.016.

[51] H. Darban, R. Luciano, A. Caporale, M. Basista, Modeling of buckling of nanobeams embedded in elastic medium by local-nonlocal stress-driven gradient elasticity theory, Composite Structures 297 (2022) 115907. https://doi.org/10.1016/j.compstruct.2022.115907.

[52] S. Wang, W. Ding, Z. Li, B. Xu, C. Zhai, W. Kang, W. Yang, Y. Li, A size-dependent quasi-3D model for bending and buckling of porous functionally graded curved nanobeam, International Journal of Engineering Science 193 (2023) 103962. https://doi.org/10.1016/j.ijengsci.2023.103962.

[53] W. Yang, S. Wang, W. Kang, T. Yu, Y. Li, A unified high-order model for size-dependent vibration of nanobeam based on nonlocal strain/stress gradient elasticity with surface effect, International Journal of Engineering Science 182 (2023) 103785. https://doi.org/10.1016/j.ijengsci.2022.103785.

[54] F.P. Pinnola, S.A. Faghidian, R. Barretta, F. Marotti de Sciarra, Variationally consistent dynamics of nonlocal gradient elastic beams, International Journal of Engineering Science 149 (2020) 103220. https://doi.org/10.1016/j.ijengsci.2020.103220.

[55] Z. Li, Y. He, J. Lei, S. Guo, D. Liu, L. Wang, A standard experimental method for determining the material length scale based on modified couple stress theory, International Journal of Mechanical Sciences 141 (2018) 198–205. https://doi.org/10.1016/j.ijmecsci.2018.03.035.

[56] D. Li, S. Li, C. Zhang, W. Chen, Propagation characteristics of shear horizontal waves in piezoelectric semiconductor nanoplates incorporating surface effect, International Journal of Mechanical Sciences 247 (2023) 108201. https://doi.org/10.1016/j.ijmecsci.2023.108201.

[57] Z. Zhang, C. Liang, D. Kong, Z. Xiao, C. Zhang, W. Chen, Dynamic buckling and free bending vibration of axially compressed piezoelectric semiconductor rod with surface effect, International Journal of Mechanical Sciences 238 (2023) 107823. https://doi.org/10.1016/j.ijmecsci.2022.107823.

[58] F. Lin, L.H. Tong, H.-S. Shen, C.W. Lim, Y. Xiang, Assessment of first and third order shear deformation beam theories for the buckling and vibration analysis of nanobeams incorporating surface stress effects, International Journal of Mechanical Sciences 186 (2020) 105873. https://doi.org/10.1016/j.ijmecsci.2020.105873.

[59] Z.Z. He, C.L. Zhang, C.Z. Zhang, W.Q. Chen, Programmable dielectric metamaterial plates via flexoelectricity and *L-C* circuits, International Journal of Mechanical Sciences 286 (2025) 109937. https://doi.org/10.1016/j.ijmecsci.2025.109937.

[60] K.S. Kumar, H. Van Swygenhoven, S. Suresh, Mechanical behavior of nanocrystalline metals and alloys1, Acta Materialia 51 (2003) 5743–5774. https://doi.org/10.1016/j.actamat.2003.08.032.

[61] T. Gao, H. Song, B. Wang, Y. Gao, Y. Liu, Q. Xie, Q. Chen, Q. Xiao, Y. Liang, Molecular dynamics simulations of tensile response for FeNiCrCoCu high-entropy alloy with voids, International Journal of Mechanical Sciences 237 (2023) 107800. https://doi.org/10.1016/j.ijmecsci.2022.107800.

[62] M. Fathalian, H. Darban, E. Postek, Atomistic insights into tensile damage of functionally Graded Al-SiC composites, International Journal of Mechanical Sciences 288 (2025) 110012. https://doi.org/10.1016/j.ijmecsci.2025.110012.

[63] A. Ghafouri Pourkermani, B. Azizi, H. Nejat Pishkenari, Vibrational analysis of Ag, Cu and Ni nanobeams using a hybrid continuum-atomistic model, International Journal of Mechanical Sciences 165 (2020) 105208. https://doi.org/10.1016/j.ijmecsci.2019.105208.

[64] J. Azadbakht, H. Nejat Pishkenari, Properly-tuned continuum and atomistic models for vibrational analysis of the silicon nanoplates, International Journal of Mechanical Sciences 229 (2022) 107517. https://doi.org/10.1016/j.ijmecsci.2022.107517.

[65] K. Mohammadi, A. Ali Madadi, Z. Bajalan, H. Nejat Pishkenari, Analysis of mechanical and thermal properties of carbon and silicon nanomaterials using a coarse-grained molecular dynamics method, International Journal of Mechanical Sciences 187 (2020) 106112. https://doi.org/10.1016/j.ijmecsci.2020.106112.

[66] H. Darban, MD benchmarks: Size-dependent tension, bending, buckling, and vibration of nanobeams, International Journal of Mechanical Sciences 296 (2025) 110316. https://doi.org/10.1016/j.ijmecsci.2025.110316.

[67] K. Nishimura, N. Miyazaki, Molecular dynamics simulation of crack growth under cyclic loading, Computational Materials Science 31 (2004) 269–278. https://doi.org/10.1016/j.commatsci.2004.03.009.

[68] Z. Yao, C.-C. Zhu, M. Cheng, J. Liu, Mechanical properties of carbon nanotube by molecular dynamics simulation, Computational Materials Science 22 (2001) 180–184. https://doi.org/10.1016/S0927-0256(01)00187-2.

[69] T. Yokoyama, M.-C. Chen, Vibration analysis of edge-cracked beams using a line-spring model, Engineering Fracture Mechanics 59 (1998) 403–409. https://doi.org/10.1016/S0013-7944(97)80283-4.

[70] A. Hassanpour, H. Darban, Softening and Stiffening Size Effects in Free Flexural Vibration of Small-Scale Cracked Beams, (2024). https://doi.org/10.2139/ssrn.4983161.

[71] S. Plimpton, Fast Parallel Algorithms for Short-Range Molecular Dynamics, Journal of Computational Physics 117 (1995) 1–19. https://doi.org/10.1006/jcph.1995.1039.

[72] F.H. Stillinger, T.A. Weber, Computer simulation of local order in condensed phases of silicon, Phys. Rev. B 31 (1985) 5262–5271. https://doi.org/10.1103/PhysRevB.31.5262.

[73] H.N. Pishkenari, B. Afsharmanesh, E. Akbari, Surface elasticity and size effect on the vibrational behavior of silicon nanoresonators, Current Applied Physics 15 (2015) 1389–1396. https://doi.org/10.1016/j.cap.2015.08.002.

[74] Montgomery, D. C., Peck, E. A., & Vining, G. G, Introduction to Linear Regression Analysis, 6th Edition, Wiley (2021), (n.d.).

[75] A. Caporale, H. Darban, R. Luciano, Nonlocal strain and stress gradient elasticity of Timoshenko nano-beams with loading discontinuities, International Journal of Engineering Science 173 (2022) 103620. https://doi.org/10.1016/j.ijengsci.2021.103620.